

Robust Denoising of Cryo-EM Images via β -GAN

Hanlin Gu^a, Ilona Christy Unarta^c, Xuhui Huang^{b,c}, Yuan Yao^{*a,c}

^a*Department of Mathematics, Hong Kong University of Science and Technology*

^b*Department of Chemistry, Center of System Biology and Human Health, State Key Laboratory of Molecular Neuroscience, Hong Kong University of Science and Technology*

^c*Department of Chemical and Biological Engineering, Hong Kong University of Science and Technology*

Abstract

The cryo-electron microscopy (Cryo-EM) becomes popular for macromolecular structure determination. However, the 2D images which Cryo-EM detects are of high noise and often mixed with multiple heterogeneous conformations and contamination, imposing a challenge for denoising. Traditional image denoising methods and simple Denoising Autoencoder can not remove Cryo-EM image noise well when the signal-noise-ratio (SNR) of images is meager and contamination distribution is complex. Thus it is desired to develop new effective denoising techniques to facilitate further research such as 3D reconstruction, 2D conformation classification, and so on. In this paper, we approach the robust denoising problem for Cryo-EM images by introducing a family of Generative Adversarial Networks (GAN), called β -GAN, which is able to achieve robust estimate of certain distributional parameters under Huber contamination model with statistical optimality. To address the challenge of robust denoising where the traditional image generative model might be contaminated by a small portion of unknown outliers, β -GANs are exploited to enhance the robustness of denoising Autoencoder. The method is evaluated by both a simulated dataset on the *Thermus aquaticus* RNA Polymerase (RNAP) and a real dataset on the *Plasmodium falciparum* 80S ribosome dataset (EMPIRE-10028), in terms of Mean Square Error (MSE), Peak Signal to Noise Ratio (PSNR), Structural Similarity Index Measure (SSIM) and 3D Reconstruction as well. The results show that equipped with some designs of β -GANs and the robust ℓ_1 -Autoencoder, one can stabilize the training of GANs and achieve the state-of-the-art performance of robust denoising with low SNR data and against possible information contamination. Our proposed methodology thus provides an effective tool for robust denoising of Cryo-EM 2D images, which is helpful for 3D structure reconstruction.

Keywords: Cryo-EM, denoising, Autoencoder, generative adversarial networks, robust statistics, 3D reconstruction

1 Introduction

The cryo-electron microscopy (Cryo-EM) has become one of the most popular techniques to resolve the atomic structure. In the past, Cryo-EM was limited to large complexes or low-

*Corresponding author

resolution models. Recently the development of new detector hardware has dramatically improved the resolution in Cryo-EM [26], which makes Cryo-EM widely used in a variety of research fields. Different from X-ray crystallography, Cryo-EM has the advantage of preventing the recrystallization of inherent water and re-contamination. Also, Cryo-EM is superior to Nuclear Magnetic Resonance spectroscopy (NMR) in solving macromolecules in the native state. In addition, both X-ray crystallography and NMR require large amounts of relatively pure samples, whereas Cryo-EM requires much fewer samples [6]. For this celebrated development of Cryo-EM for the high-resolution structure determination of biomolecules in solution, the Nobel Prize in Chemistry in 2017 was awarded to three pioneers in this field [38].

However, it is a computational challenge in processing raw Cryo-EM images, due to heterogeneity in molecular conformations and high noise. Macromolecules in natural conditions are usually heterogeneous, i.e., multiple metastable structures may coexist in the experimental samples [15, 37]. Such conformational heterogeneity adds extra difficulty to the structural reconstruction as we need to assign each 2D image to not only the correct projection angle but also its corresponding conformation. This imposes a computational challenge that one needs to denoise

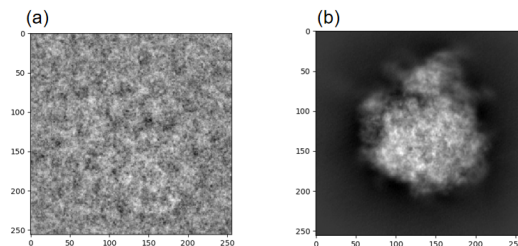


Figure 1: (a) a noisy Cryo-EM image (b) a reference image

the Cryo-EM images without losing the key features of their corresponding conformations. Moreover, in the process of generating Cryo-EM images, one needs to provide a view using the electron microscope for samples that are in frozen condition. Thus there are two types of noise: one is from ice, and the other is from the electron microscope. Both of them are significant in contributing high noise in Cryo-EM images and leave a difficulty to the detection of particle structures (Figure 1 shows a typical noisy Cryo-EM image with its reference image which is totally non-identifiable to human eyes). In extreme cases, some experimental images even do not contain any particles, rendering it difficult for particle picking either manually or automatically [43]. How to achieve robust denoising against such kind of contamination thus becomes a critical problem. So it is a great challenge to develop robust denoising methods for Cryo-EM images to reconstruct heterogeneous biomolecular structures.

There are a plethora of denoising methods developed in applied mathematics and machine learning that could be applied to Cryo-EM image denoising. Most of them in Cryo-EM are based on unsupervised learning, which don't need any reference image data to learn. [44] proposed a filtering method based on non-local means, which makes use of the rotational symmetry of some biological molecules. Also, [46] designed the adaptive non-local filter, which takes advantage of a wide range of pixels to estimate the denoised pixel values. Besides, [48] compared transform domain filtering method: BM3D [13] and dictionary learning method: KSVD [2] in denoising problem in Cryo-EM. However, all of these do not work well in low Signal-Noise-Ratio (SNR) situations like Cryo-EM. In addition, Covariance Wiener Filtering (CWF) [8] is proposed for image denoising. It demonstrates that CWF needs large sample size of data in order to estimate the covariance matrix correctly, although it has an attractive denoising effect.

Deep learning technique has entered the field of image denoising with its rapid progress

in image classification. One of the most popular methods is denoising Autoencoder (DA) motivated by [42] that needs reference data to learn a compressive representation (encoding) for a set of data. The extension of DA in [49] exploits sparsity regularization in addition to the reconstruction loss in order to avoid overfitting. Other developments such as [51] takes advantage of the residual network architecture and [1] combines several sparse denoising Autoencoder directed to be robust to different noise. However, deep Autoencoders have not been applied to Cryo-EM denoising up to our knowledge.

On the other hand, Generative Adversarial Networks (GAN) recently gains its popularity in machine learning field and provides a promising new approach for Cryo-EM image denoising. The modern version of GAN proposed in [18] is mainly composed of two parts: generator (G : generate the new samples) and discriminator (D : determine whether the samples are real or generated (fake)). In pursuit of a minimax zero-sum game, it aims to minimize the Jensen-Shannon (JS) divergence between distributions of generated samples and true samples, hence called JS-GAN. Various GANs are then studied, and in particular, [3] proposed WGAN, which uses Wasserstein distance in replacement of the JS divergence. [19] further improved WGAN with the addition of the gradient penalty that makes the training more stable. For image denoising, [50] applied GAN to medical image denoising in the low noise situation. In particular, [39] applied JS-GAN to Cryo-EM image denoising in a homogeneous molecular setting. Recently, [16, 17] showed that a general family of GANs (β -GANs, including JS-GAN and TV-GAN, etc.) enjoys robust reconstruction when the data set contain outliers under Huber contamination models. Therefore, such GANs equip us with a natural technique for robust denoising for Cryo-EM images, which becomes the central topic in this paper.

In this paper, we investigate a robust denoising of Cryo-EM images based on joint training of β -GANs and denoising Autoencoders. In particular, our main contributions are as follows.

- In order to better describe the complex generative process in Cryo-EM images, we enhance the traditional image generative model with Huber contamination model, where a small portion of samples allows for unknown contamination. To recover the clean image in this new model, we introduce a family of β -GAN, which is able to achieve the robustness of denoising against partial contamination of samples (e.g., (.5, .5)-GAN or (1, 1)-GAN ¹ in this family work best in this paper).
- We exploit a joint training of GANs and denoising Autoencoders toward robust denoising. Both Autoencoder and GANs help each other for Cryo-EM denoising in low signal-noise-ratio scenarios. On the one hand, Autoencoder helps stabilize GANs during training, without which the training processes of GANs are often collapsed due to high noise; on the other hand, GANs help Autoencoder in denoising by sharing information in similar samples via distribution learning and enhancing the robustness against contaminations.
- Numerical experiments and reconstruction are conducted with both simulated dataset on the *Thermus aquaticus* RNA Polymerase (RNAP) and a real dataset on the *Plasmodium falciparum* 80S ribosome dataset (EMPIRE-10028). The experiments on those

¹ β -GAN has two parameters: α and β , written as (α, β) -GAN, see details in 2.1.

datasets show the validity of the proposed methodology and suggest that: some designs of β -GANs, such as (.5, .5)-GAN and (1, 1)-GAN, joint with robust ℓ_1 -Autoencoder are among the best choices in robust denoising against unknown contamination; on the other hand, despite that WGANs achieve superb performance in contamination-free scenarios, they deteriorate significantly under contaminated samples.

The organization of this paper is as follows. Section 2 introduces the methodology; Section 3 reports the experimental results; discussion and conclusion are given in Section 4.

2 Methodology

2.1 A Generative Model with Huber Contamination

Let $x \in \mathbb{R}^{d_1 \times d_2}$ be a clean image, often called reference image in the sequel. The generative model of noisy image $y \in \mathbb{R}^{d_1 \times d_2}$ in cryo-EM under the linear, weak phase approximation [14, 8] can be described by

$$y = a * x + \zeta \quad (1)$$

where $*$ denotes the convolution operation, a is the point spread function of the microscope convolving with the clean image and ζ is an additive noise, usually assumed to be Gaussian noise that corrupts the image. In order to remove the noise the microscope brings, traditional Denoising Autoencoder such as [5] could be exploited to learn from examples $(y_i, x_i)_{i=1, \dots, n}$ the inverse mapping a^{-1} from the noisy image y to the clean image x .

However, this model is not sufficient in the real case in Cryo-EM. In the experimental data, Cryo-EM images are possibly contaminated by the ice or others, which do not contain any interesting particle information. For example, particles don't exist in all Cryo-EM images, such that even the experimentalists do the manual or automatic particle picking [43]. Such contaminations will significantly affect our denoising efficiency if the denoising methods continuously depend on the sample outliers. Therefore we introduce the following Huber contamination model to extend the image formation model of Equation (1).

Consider that the pair of reference image and experimental image (x, y) is subject to the following mixture distribution P_ϵ :

$$P_\epsilon = (1 - \epsilon)P_0 + \epsilon Q, \quad \epsilon \in [0, 1], \quad (2)$$

a mixture of true distribution P_0 of probability $(1 - \epsilon)$ and arbitrary contamination distribution Q of probability ϵ . P_0 is characterized by model (1) and Q accounts for the unknown contamination distribution possibly due to ice, broken of data, and so on such that the image sample does not contain any particle information. This is called the Huber contamination model in statistics [20]. Our purpose is that given n samples $(x_i, y_i) \sim P_\epsilon$ ($i = 1, \dots, n$), possibly contaminated with unknown Q , learn a robust inverse map $a^{-1}(y)$.

2.2 Robust Denoising Method

In this report, we exploit a neural network to approximate the robust inverse mapping $G_\theta : \mathbb{R}^{d_1 \times d_2} \rightarrow \mathbb{R}^{d_1 \times d_2}$, here a neural network parameterized by $\theta \in \Theta$ whose structure will be discussed in Section 3. Our goal is to ensure that discrepancy between reference image x

and reconstructed image $\hat{x} = G_\theta(y)$ is small. Such a discrepancy is usually measured by some non-negative loss function: $\ell(x, \hat{x})$. Therefore, the denoising problem minimizes the following expected loss,

$$\arg \min_{\theta \in \Theta} \mathcal{L}(\theta) := \mathbb{E}_{x,y}[\ell(x, G_\theta(y))] \quad (3)$$

In practice, given a set of training samples $S = \{(x_i, y_i) : i = 1, \dots, n\}$, we aim to solve the following empirical loss minimization problem,

$$\arg \min_{\theta \in \Theta} \hat{\mathcal{L}}_S(\theta) := \frac{1}{n} \sum_{i=1}^n \ell(x_i, G_\theta(y_i)) \quad (4)$$

For example, the following choices of loss functions will be considered in this paper:

- (**ℓ_2 -Autoencoder**) $\ell(x, \hat{x}) = \frac{1}{2} \|x - \hat{x}\|_2^2 := \frac{1}{2} \sum_{i,j} (x_{ij} - \hat{x}_{ij})^2$, or equivalently $\mathbb{E} \ell(x, \hat{x}) = D_{KL}(p(x) \| q(\hat{x}_\theta))$ where $\hat{x}_\theta \sim \mathcal{N}(x, \sigma^2 I_D)$;
- (**ℓ_1 -Autoencoder**) $\ell(x, \hat{x}) = \|x - \hat{x}\|_1 := \sum_{i,j} |x_{ij} - \hat{x}_{ij}|$, or equivalently $\mathbb{E} \ell(x, \hat{x}) = D_{KL}(p(x) \| q(\hat{x}_\theta))$ where $\hat{x}_\theta \sim \text{Laplace}(x, b)$;
- (**Wasserstein-GAN**) $\ell(x, \hat{x}) = W_1(p(x), q_\theta(\hat{x}))$ where W_1 is the 1-Wasserstein distance between distributions of x and \hat{x} ;
- (**β -GAN**) $\ell(x, \hat{x}) = D(p(x) \| q_\theta(\hat{x}))$ where D is some divergence function to be discussed below between distributions of x and \hat{x} .

Both the ℓ_2 and ℓ_1 losses consider the reconstruction error of G_θ . The ℓ_2 -loss above is equivalent to assume that $G_\theta(y|x)$ follows a Gaussian distribution $\mathcal{N}(x, \sigma^2 I_D)$, and the ℓ_1 -loss instead assumes a Laplacian distribution centered at x . As a result, the ℓ_2 -loss pushes the reconstructed image \hat{x} toward mean by averaging out the details and thus blurs the image. On the other hand, the ℓ_1 -loss pushes \hat{x} toward the coordinate-wise median, keeping the majority of details while ignoring some large deviations, thus increases the contrast of the reconstructed image and becomes more robust than the ℓ_2 loss against large outliers. Although ℓ_1 -Autoencoder has a more robust loss than ℓ_2 , both of them are not sufficient to handle the contamination in (2). To deal with the Huber contamination model (2), β -GAN will be introduced below.

2.2.1 β -GAN

Recently [16, 17] showed that some types of GANs might achieve robustness for Huber contamination models, playing a similar role as Tukey’s median [41] in terms of statistical optimality. Therefore it is natural to bring such robust GANs into our considerations. In particular, the following so called β -GAN is shown in [17] to achieve statistically optimal robust estimates.

Adapted to the setting in this paper, β -GAN aims to solve the following minimax optimization problem to find the G_θ ,

$$\min_{G_\theta} \max_D \mathbb{E}[S(D(x), 1) + S(D(G_\theta(y)), 0)] \quad (5)$$

where $S(t, 1) = -\int_t^1 c^{\alpha-1}(1-c)^\beta dc$, $S(t, 0) = -\int_0^t c^\alpha(1-c)^{\beta-1} dc$, $\alpha, \beta \in [-1, 1]$, and D is another neural network called discriminator whose architecture will be discussed in Section 3 on Results. For simplicity, we denote this family with parameters α, β by (α, β) -GAN in this paper.

The family of (α, β) -GAN includes many popular members. For example, when $\alpha = 0, \beta = 0$, it becomes the JS-GAN [18] which aims to solve the following minimax problem whose loss is the Jensen-Shannon divergence,

$$\min_{G_\theta} \max_D \mathbb{E}_{(x,y) \sim P(X,Y)} \{\log(D(x)) + \log(1 - D(G_\theta(y)))\}. \quad (6)$$

When $\alpha = 1, \beta = 1$ the loss is a simple mean square loss; when $\alpha = -0.5, \beta = -0.5$, the loss is boost score. In particular, it is shown in [17] that for all $|\alpha - \beta| < 1$, (α, β) -GAN family is robust in the sense that one can learn an elliptical distribution P_0 from contaminated distributions P_ϵ under the strong contamination model:

$$\{P_\epsilon \in \mathcal{P}(X, Y) : TV(P_\epsilon, P_0) \leq \epsilon\}. \quad (7)$$

More details can be seen in Appendix 5.1. In this report, we are going to see such β -GANs can also help enhance the robustness of Cryo-EM image denoising against contamination.

Yet, we note that Wasserstein GAN (WGAN) is not a member of this family. By formally taking $S(t, 1) = t$ and $S(t, 0) = -t$, we have the following WGAN where an additional gradient penalty is added here (WGANgp) [19, 3].

$$\min_G \max_D \mathbb{E}_{(x,y) \sim P(X,Y)} \{D(x) - D(G(y)) + \mu \mathbb{E}_{\tilde{x}} (\|\nabla_{\tilde{x}} D(\tilde{x})\|_2 - 1)^2\} \quad (8)$$

where \tilde{x} is uniformly sampled along straight lines connecting pairs of generated and real samples; and μ is a weighting parameter. In WGANgp, the last layer of the sigmoid function in the discriminator network is removed. Thus D 's output range is the whole real \mathbb{R} , but its gradient is close to 1 to achieve Lipschitz-1 functions. Gradient penalty may help stabilize the training of WGAN. Compared to JS-GAN, WGAN aims to minimize the Wasserstein distance between the sample distribution and the generator distribution. Therefore, WGAN is not robust in the sense of contamination models above as arbitrary ϵ portion of outliers can be far away from the main distribution P_0 such that the Wasserstein distance is arbitrarily large.

2.2.2 Joint Autoencoder-GAN and Main Algorithm

Cryo-EM images consist of 2D-projections of the same molecular conformation in different viewing angles, and the reconstruction losses (ℓ_1 or ℓ_2) do not explicitly take into account similar images of similar conformational projections. However in addition to possible robustness, GANs can further help denoising by exploiting common information in similar samples during distribution learning; for example, they minimize some divergence or Wasserstein distance between reference image set and denoised image set where similar images can help boost signals for each other.

On the other hand, Autoencoder can help stabilize GANs during training, without which the training processes of GANs are often oscillating and sometimes collapsed due to the presence of high noise (see Appendix 5.2).

For these considerations, in this paper, we propose a combined loss with both GAN and Autoencoder reconstruction loss,

$$\widehat{\mathcal{L}}_{GAN}(x, \widehat{x}) + \lambda \|x - \widehat{x}\|_p^p$$

where $p \in \{1, 2\}$ and $\lambda \geq 0$ is a trade-off parameter for ℓ_p reconstruction loss. Algorithm 1 summarizes the procedure of joint training of Autoencoder and GAN, which will be denoted as “GAN+ ℓ_p ” in the experimental section depending on the proper choice of GAN and p .

Algorithm 1 Joint training of (α, β) -GAN and ℓ_p -Autoencoder.

Input:

1. (α, β) for $S(t, 1) = -\int_t^1 c^{\alpha-1}(1-c)^\beta dc$, $S(t, 0) = -\int_0^t c^\alpha(1-c)^{\beta-1} dc$
or $S(t, 1) = t$, $S(t, 0) = -t$ for WGAN
2. λ regularization parameter of the ℓ_p -Autoencoder
3. k_d number of iterations for discriminator, k_g number of iterations for generator
4. η_d learning rate of discriminator, η_g learning rate of generator
5. ω weights of discriminator, θ weights of generator
- 1: **for** number of training iterations **do**
- 2: • Sample minibatch of m examples $\{(x^{(1)}, y^{(1)}), \dots, (x^{(m)}, y^{(m)})\}$ from reference-noisy image pairs.
- 3: **for** $k = 1, 2, \dots, k_d$ **do**
- 4: • Update the discriminator by gradient ascent:
- 5: $g_\omega \leftarrow \frac{1}{m} \sum_{i=1}^m \nabla_\omega [S(D_\omega(x_i), 1) + S(D_\omega(G_\theta(y_i)), 0) + \mu(\|\nabla_{\widehat{x}} D_\omega(\widehat{x}_i)\|_2 - 1)^2]$
 where $\mu > 0$ for WGANgp only;
- 6: $\omega \leftarrow \omega + \eta_d g_\omega$
- 7: **end for**
- 8: **for** $k = 1, 2, \dots, k_g$ **do**
- 9: • Update the generator by gradient descent:
- 10: $g_\theta \leftarrow \frac{1}{m} \sum_{i=1}^m \nabla_\theta [S(D_\omega(G_\theta(y_i)), 0) + \lambda |G_\theta(y_i) - x_i|^p]$, $p \in \{1, 2\}$;
- 11: $\theta \leftarrow \theta - \eta_g g_\theta$
- 12: **end for**
- 13: **end for**

Return: Denoised image: $\widehat{x}_i = G_\theta(y_i)$

2.3 Evaluation Method

We exploit the following three metrics to determine whether the denoising result is good or not. They are the Mean Square Error (MSE), the Peak Signal-to-Noise Ratio (PSNR) and the Structural Similarity Index Measure (SSIM).

- (MSE) For images of size $d_1 \times d_2$, the Mean Square Error (MSE) between reference image x and denoised image \widehat{x} is defined as, $MSE := \frac{1}{d_1 d_2} \sum_{i=1}^{d_1} \sum_{j=1}^{d_2} (x(i, j) - \widehat{x}(i, j))^2$. The smaller is the MSE, the better the denoising result is.
- (PSNR) Similarly, the Peak Signal-to-Noise Ratio (PSNR) between reference image x and denoised image \widehat{x} whose pixel value range is $[0, t]$ (1 by default), is defined by $PSNR := 10 \log_{10} \frac{t^2}{\frac{1}{d_1 d_2} \sum_{i=1}^{d_1} \sum_{j=1}^{d_2} (x(i, j) - \widehat{x}(i, j))^2}$. The larger is the PSNR, the better the denoising result is.
- (SSIM) The third criterion is the Structural Similarity Index Measure (SSIM) between reference image x and denoised image \widehat{x} is defined in [45], $SSIM = \frac{(2\mu_x \mu_{\widehat{x}} + c_1)(2\sigma_x \sigma_{\widehat{x}} + c_2)(\sigma_{x\widehat{x}} + c_3)}{(\mu_x^2 + \mu_{\widehat{x}}^2 + c_1)(\sigma_x^2 + \sigma_{\widehat{x}}^2 + c_2)(\sigma_x \sigma_{\widehat{x}} + c_3)}$.

where μ_x ($\mu_{\hat{x}}$) and σ_x ($\sigma_{\hat{x}}$) are the mean and variance of x (\hat{x}), respectively, $\sigma_{x\hat{x}}$ is covariance of x and \hat{x} , $c_1 = K_1L^2$, $c_2 = K_2L^2$, $c_3 = \frac{c_2}{2}$ three variables to stabilize the division with weak denominator ($K_1 = 0.01$, $K_2 = 0.03$ by default), L is the dynamic range of the pixel-value (1 by default). The value SSIM of lies in $[0, 1]$, where the closer it is to 1, the better the result is.

Although these metrics are widely used in image denoising, we note that they might not be the best metrics for Cryo-EM images. For example, Appendix 5.7 shows an example that the best-reconstructed images perhaps do not meet the best MSE/PSNR/SSIM metrics.

In addition to these metrics, we consider the 3D reconstruction based on denoised images. Particularly, we take the 3D reconstruction by RELION [36] to validate the denoised result. The procedure of our RELION reconstruction is as follows: firstly creating the 3D initial model, then doing 3D classification, followed by operating 3D auto-refine. Moreover, for heterogeneous conformations in simulation data, we further turn the denoising results into a clustering problem to measure the efficacy of denoising methods, whose details will be discussed in Appendix 5.4.

2.4 RNAP: Simulation Dataset

We design a conformational heterogeneous dataset obtained by simulations. We use *Thermus aquaticus* RNA Polymerase (RNAP) in complex with σ^A factor (*Taq* holoenzyme) for our dataset. RNAP is the enzyme that transcribes RNA from DNA (transcription) in the cell. During the initiation of transcription, the holoenzyme must bind to the DNA, then separate the double-stranded DNA into single-stranded [9]. *Taq* holoenzyme has a crab-claw like structure, with two flexible domains, the clamp and β pincers. The clamp, especially, has been suggested to play an important role in the initiation, as it has been captured in various conformations by CryoEM during initiation [10]. Thus, we focus on the movement of the clamp in this study. To generate the heterogeneous dataset, we start with two crystal structures of *Taq* holoenzyme, which vary in their clamp conformation, open (PDB ID: 1L9U [31]) and closed (PDB ID: 4XLN [4]) clamp. For the closed clamp structure, we remove the DNA and RNA in the crystal structure, leaving only the RNAP and σ^A for our dataset. The *Taq* holoenzyme has about 370 kDa molecular weight. We then generate the clamp intermediate structures between the open and closed clamp using multiple-basin coarse-grained (CG) molecular dynamic (MD) simulations (citepokazaki2006multiple,kenzaki2011cafemol). CG-MD simulations simplify the system such that the atoms in each amino acid are represented by one particle. The structures from CG-MD simulations are refined back to all-atom or atomic structures using PD2 ca2main (citepmoore2013high) and SCRWL4 (citepkrivov2009improved). Five structures with equally-spaced clamp opening angle are chosen for our heterogeneous dataset (shown in Figure 2). Then, we convert the atomic structures to $128 \times 128 \times 128$ volumes using Xmipp package [29] and generate the 2D projections with an image size of 128×128 pixels. We further contaminate those clean images with additive Gaussian noise at different signal noise ratios (SNR): $SNR = 0.05$. The SNR is defined by “ $SNR = \text{Var}(\text{Signal})/\text{Var}(\text{Noise})$ ” in the real space. For simplicity, we did not apply the contrast transfer function (CTF) to the datasets, and all the images are centered. Figure 2 shows the five conformations pictures.

Training data size is 25000 paired images(noisy and reference images), Test data to

calculate the MSE, PSNR and SSIM is another 1500 paired images.

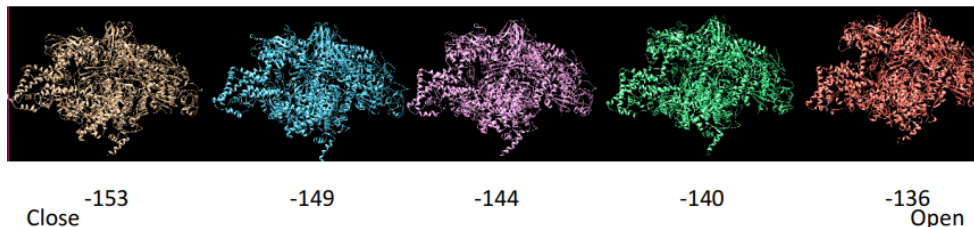


Figure 2: Five conformations in RNAP heterogeneous dataset, from left to right are close conformation to open conformation of different angles.

2.5 EMPIAR-10028: Real Dataset

This is a real-world experimental dataset that was firstly studied in [47]: the *Plasmodium falciparum* 80S ribosome dataset (EMPIAR-10028). They recover the Cryo-EM structure of the cytoplasmic ribosome from the human malaria parasite, *Plasmodium falciparum*, in complex with emetine, an anti-protozoan drug, at 3.2\AA resolution. Ribosome is the essential enzyme that translates RNA to protein molecules, the second step of central dogma. The inhibition of ribosome activity of *Plasmodium falciparum* would effectively kill the parasite [47]. We can regard this dataset to have homogeneous property. This dataset contains 105247 noisy particles with an image size of 360×360 pixels. In order to decrease the complexity of the computing, we pick up the center square of each image with a size of 256×256 , since the surrounding area of the image is entirely useless that does not lose information in such a preprocessing. Then the 256×256 images are fed as the input of the G_θ -network (Figure 3). Since the GAN-based method needs clean images as reference, we prepare their clean counterparts in the following way: we first use cryoSPARC1.0 [34] to build a 3.2\AA resolution volume and then rotate the 3D-volume by the Euler angles obtained by cryoSPARC to get projected 2D-images. The training data size we pick is 19500, and the test data size is 500.

3 Results

3.1 Network Architecture and Hyperparameter

In the experiments of this paper, the best results come from the ResNet architecture [39] shown in Figure 3, which has been successfully applied to study biological problems such as predicting protein-RNA binding. The generator in such GANs exploits the Autoencoder network architecture, while the discriminator is a binary classification ResNet. In Appendix 5.5 and 5.6, we also discuss a Convolutional Network without residual blocks and the PGGAN [21] architecture with their experimental results, respectively.

We chose Adam [23] for the Optimization. The learning rate of the discriminator is $\eta_d = 0.001$, and the learning rate of the generator is $\eta_g = 0.01$. We choose $m = 20$ as our batch size, $k_d = 1$, and $k_g = 2$ in Algorithm 1.

For (α, β) -GAN, we reports two types of choices: (1) $\alpha = 1, \beta = 1$; (2) $\alpha = 0.5, \beta = 0.5$ since they show the best results in our experiments, while the others are collected in Appendix

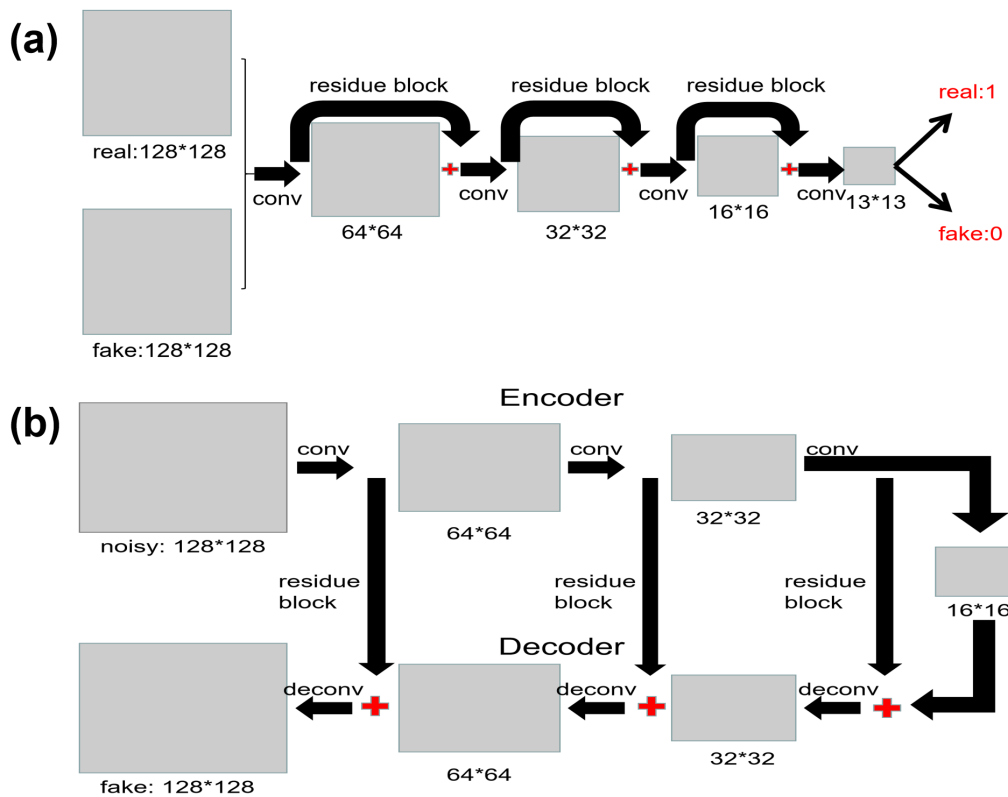


Figure 3: The architectures of (a) discriminator (D) and (b) generator (G) which borrow the residue structure. The input image size (128×128) here is adapted to RNAP dataset, while in EMPIRE-10028 dataset it is 256×256 with a similar architecture.

Table 1: Denoising result without contamination in simulated RNAP dataset: MSE, PSNR and SSIM of different models, such as BM3D [13], KSVD [2], Non-local means [46], CWF [8], DA and GAN-based methods.

Method/SNR	MSE		PSNR		SSIM	
	0.1	0.05	0.1	0.05	0.1	0.05
BM3D	3.52e-2 (7.81e-3)	5.87e-2(9.91e-3)	14.54(0.15)	12.13(0.14)	0.20(0.01)	0.08(0.01)
KSVD	1.84e-2(6.58e-3)	3.49e-2(7.62e-3)	17.57(0.16)	14.61(0.14)	0.33(0.01)	0.19(0.01)
Non-local means	5.02e-2(5.51e-3)	5.81e-2(8.94e-3)	13.04(0.50)	12.40(0.65)	0.18(0.01)	0.09(0.01)
CWF	2.53e-2(2.03e-3)	9.28e-3(8.81e-4)	16.06(0.33)	20.31(0.41)	0.25(0.01)	0.08(0.01)
ℓ_2 -Autoencoder ²	3.13e-3(7.97e-5)	4.02e-3(1.48e-4)	25.10(0.11)	23.67(0.77)	0.79(0.02)	0.79(0.01)
ℓ_1 -Autoencoder ³	3.16e-3(7.05e-5)	4.23e-3(1.32e-4)	25.05(0.09)	23.80(0.13)	0.77(0.02)	0.76(0.01)
(0, 0)-GAN + ℓ_1 ⁴	3.06e-3(5.76e-5)	4.02e-3(5.67e-4)	25.25(0.04)	24.00(0.06)	0.78(0.03)	0.78(0.03)
WGAN _{gp} + ℓ_1	2.95e-3(1.41e-5)	4.00e-3(8.12e-5)	25.42(0.04)	24.06(0.05)	0.83(0.02)	0.80(0.03)
(1, 1)-GAN + ℓ_1	2.99e-3(3.51e-5)	4.01e-3(1.54e-4)	25.30(0.05)	24.07(0.16)	0.82(0.03)	0.79(0.03)
(.5, .5)-GAN + ℓ_1	3.01e-3(2.81e-5)	3.98e-3(4.60e-5)	25.27(0.04)	24.07(0.05)	0.79(0.04)	0.80(0.03)

5.3. For WGAN, the gradient penalty with parameter $\mu = 10$ is used to accelerate the speed of convergence and hence the algorithm is denoted as WGAN_{gp} below. The trade-off (regularization) parameter of ℓ_1 or ℓ_2 reconstruction loss is set to be $\lambda = 10$ through out this section, while an ablation study on varying λ is discussed in Appendix 5.7.

3.2 Results for RNAP

3.2.1 Denoising without contamination

In this part, we attempt to denoise the noisy image without the contamination (i.e., $\epsilon = 0$ in model (2)). In order to present the advantage of GAN, we compare the denoising result in different methods. Table 1 shows the MSE and PSNR of different methods in SNR 0.05 and 0.1. We recognize the traditional methods such as KSVD, BM3D, Non-local mean, and CWF can remove the noise partially and extract the general outline, but they still leave the unclear piece. However, deep learning methods can perform much better. Specifically, we observe that GAN-based methods, especially WGAN_{gp} + ℓ_1 loss and (.5, .5)-GAN + ℓ_1 loss, perform better than denoising Autoencoder methods, which only optimizes ℓ_1 or ℓ_2 loss. The adversarial process inspires the generation process, and the additional ℓ_1 loss optimization speeds up the process of generation towards reference images. Notably, WGAN_{gp} and (5, .5)- or (1, 1)-GANs are among the best methods, where the best mean performance up to one standard deviation are all marked in bold font. Specifically, compared with (.5, .5)-GAN, the WGAN_{gp} get better PSNR and SSIM in SNR 0.1; the (.5, .5)-GAN shows the advantage in PSNR and SSIM in SNR 0.05 while (1, 1)-GAN is competitive within one standard deviation. Also, Figure 4(a) presents the denoised images of denoising methods in SNR 0.05. For the convenience of comparison, we choose a clear open-conformation to present, and the performances show that WGAN_{gp} and (α, β) -GAN can grasp the “open” shape completely and derive the more explicit pictures than other methods.

What’s more, in order to test the denoised results of β -GAN, we reconstruct the 3D volume by RELION in 200000 images of SNR 0.1, which are denoised by (.5, .5)-GAN + ℓ_1 . The value of pixel size, amplitude contrast, spherical aberration and voltage are 1.6, 2.26, 0.1 and 300. For the other terms, retaining the default settings in RELION software. Figure 4(b) and (c) separately show the 3D volume recovered by clean images and denoised

² ℓ_2 -Autoencoder represents ℓ_2 loss

³ ℓ_1 -Autoencoder represents ℓ_1 loss

⁴GAN + ℓ_1 represents adding ℓ_1 regularization in GAN generator loss

images. Also, the related FSC curves are shown in Figure 4(d). Specifically, the blue curve, which represents (.5, .5)-GAN + ℓ_1 denoised images is closed to red curves representing the clean images. We use the 0.143 cutoff criterion in literature (the resolution as Fourier shell correlation reaches 0.143, shown by dash lines in Figure 4(d)) to choose the final resolution: 3.39Å. The structure recovered by our method and FSC curve are as good as the original structure, which illustrates that the denoised result of β -GAN can identify the details of image and be helpful in 3D reconstruction.

In addition, Appendix 5.4 also shows an example that GAN with ℓ_1 -Autoencoder helps heterogeneous conformation clustering.

3.2.2 Robustness under contamination

In this part, we consider the contamination model $\epsilon \neq 0$ and Q from purely noisy images. We randomly replace partial samples of our training dataset of RNAP by noise to test whether our model is robust or not. There are three ways to test: (A) Only replacing the clean reference images. It implies the reference images are wrong or missing, such that we do not have the reference images to compare. This is the worst contamination case. (B) Only replacing the noisy images. It means the Cryo-EM images the machine produces are broken. (C) Replacing both, which indicates both A and B happen. The latter two are mild contamination cases, especially C that replaces both reference and noisy images by Gaussian noise whose ℓ_1 or ℓ_2 loss is thus well-controlled.

Here we test our robustness of various deep learning based methods using the data of SNR 0.1, and the former three contaminations are applied to randomly replace the samples in the proportion of $\epsilon \in \{0.1, 0.2, 0.3\}$ of the whole dataset.

Figure 4(e), (f) and (g) compare the robustness of different methods. In all the cases, some β -GANs ((.5, .5)- and (1, 1)-) with ℓ_1 -Autoencoder exhibit relatively universal robustness. Particularly, (1) The MSE with ℓ_1 loss is less than the MSE with ℓ_2 loss, which represents the ℓ_1 loss is more robust than ℓ_2 as desired. (2) The Autoencoder method in ℓ_2 loss and WGANgp show certain robustness in case B and C but are largely influenced by contamination in case A (shown in Figure 4 (e)), indicating the most serious damage arising from type A, merely replacing only the reference image by Gaussian noise. The reason is that the ℓ_2 Autoencoder and WGANgp method are confused by the wrong reference images so that they can not learn the mapping from data distribution to reference distribution accurately. (3) In the type C, the standard deviations of the five best models are larger compared the other two types. The contamination of both noisy y and clean x images influence the the stability of model more than the other two types.

Furthermore, we take an example in type A contamination with $\epsilon = 0.1$ for 3D reconstruction. The 3D reconstruction in denoised images with (.5, .5)-GAN + ℓ_1 and ℓ_2 -Autoencoder are shown in Figure 4(h) and (j), and related FSC curve is Figure 4(i). Specifically, on the one hand, the blue FSC curve of ℓ_2 -Autoencoder doesn't drop, which leads to the worse reconstruction; on the other hand, the red FSC curve of (.5, .5)-GAN + ℓ_1 drops quickly but begins to rise again, whose reason is that some unclear detail of structure mixed angular information in reconstruction. When applying 0.143 cutoff criterion (dashed line in FSC curve), the resolution of (.5, .5)-GAN + ℓ_1 is about 4Å. Although reconstruction of images and final resolution is not better than the clean images, it is much clearer than ℓ_2 -Autoencoder which totally fails in the contamination case. The outcome of the reconstruction

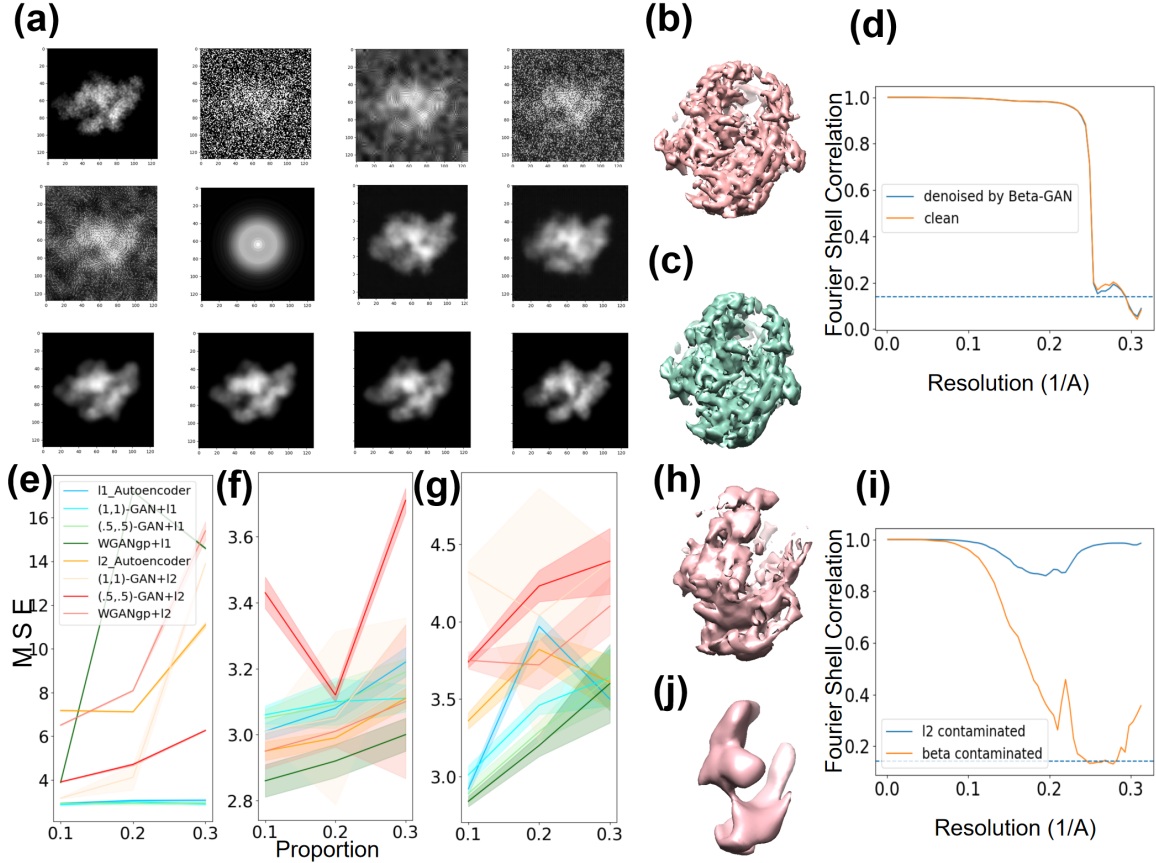


Figure 4: Results for RNAP dataset. (a) is denoised images in different denoised methods (from left to right, top to bottom): Clean, Noisy, BM3D, KSVD, Non-local means, CWF, ℓ_1 -Autoencoder, ℓ_2 -autoencoder, (1,1)-GAN + ℓ_1 , (0,0)-GAN + ℓ_1 , (.5, .5)-GAN + ℓ_1 and WGANgp + ℓ_1 . (b) and (c) are reconstruction of clean images and (.5, .5)-GAN + ℓ_1 denoised images. (d) is FSC curve of (b) and (c). (e), (f) and (g) are robustness tests of various methods under $\epsilon \in \{0.1, 0.2, 0.3\}$ -proportion contamination in three types of contamination: (e) Type A: replacing the reference images with random noise; (f) Type B: replacing the noisy images with random noise; (g) Type C: replacing both with random noise. (h) and (j) are reconstructions of images with (.5, .5)-GAN + ℓ_1 and ℓ_2 -autoencoder under type A contamination, respectively, where ℓ_2 -autoencoder totally fails but (.5, .5)-GAN + ℓ_1 is robust. (i) shows FSC curves of (h) and (j).

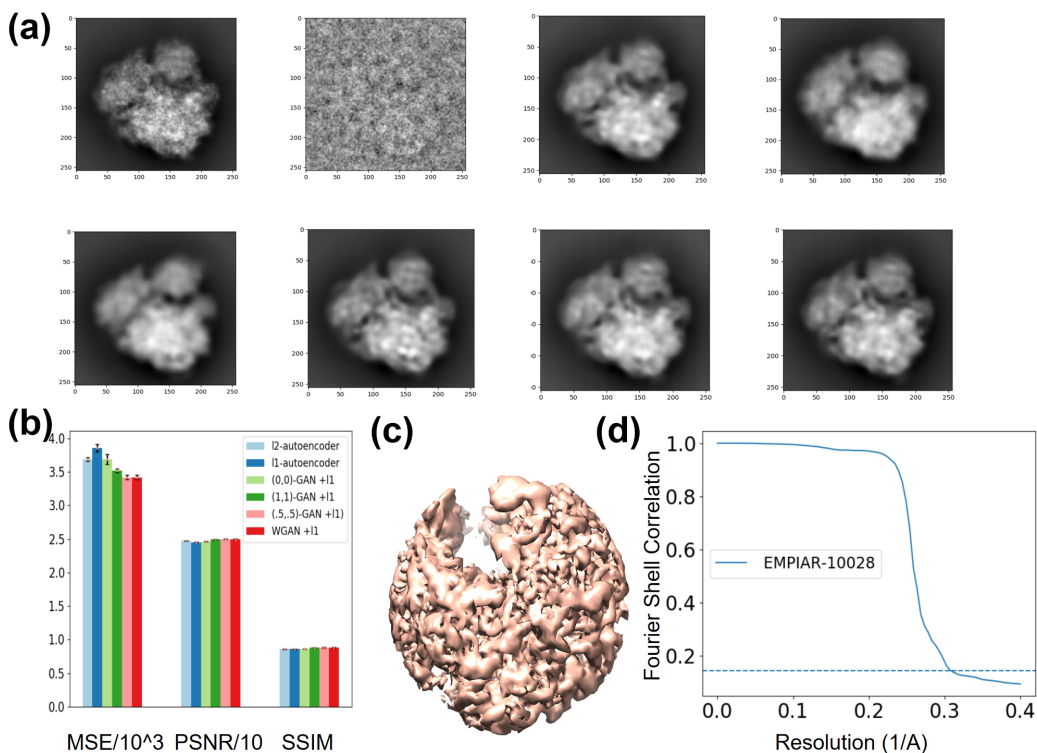


Figure 5: Results for EMPIRE-10028. (a) Comparison in EMPIRE-10028 dataset in different deep learning methods (from left to right, top to bottom): clean image, noisy image, ℓ_1 -Autoencoder, ℓ_2 -Autoencoder, (0,0)-GAN + ℓ_1 , (1,1)-GAN + ℓ_1 , (.5, .5)-GAN + ℓ_1 , WGANgp + ℓ_1 . (b) is the MSE, PSNR and SSIM in different denoised methods. (c) and (d) is the 3D-reconstruction of denoised images by (.5, .5)-GAN + ℓ_1 and the FSC curve, respectively. The resolution of reconstruction from (.5, .5)-GAN + ℓ_1 denoised images is 3.20Å, which is as good as the original resolution.

demonstrates that (.5, .5)-GAN + ℓ_1 is relatively robust, whose 3D result is consistent with the clean image reconstruction.

In a summary, some (α, β) -GANs ((.5, .5) and (1, 1) here) with ℓ_1 Autoencoder are more resistant to sample contamination, which are better to be applied into the Cryo-EM experimental data.

3.3 Denoising and Reconstruction Results for EMPIRE-10028

The following Figure 5(a) and (b) show the denoising results by different deep learning methods in experimental data: ℓ_1 or ℓ_2 Autoencoders, JS-GAN ((0, 0)-GAN), WGANgp, and (α, β) -GAN, where we add ℓ_1 loss in all of the GAN-based structures. Although the Autoencoder can grasp the shape of macromolecules, it is a little blur in some parts. What is more, WGANgp and (α, β) -GAN can perform well. According to MSE and PSNR, WGANgp and (.5, .5)-GAN perform better than other deep learning methods, largely consistent with the result of the RNAP dataset. The improvements of such GANs over pure Autoencoders

lie in their ability of utilizing structural information among similar images to learn the data distribution better.

Finally, we take reconstruction via RELION of 100000 images, which denoised by (.5, .5)-GAN + ℓ_1 . The parameters are the same as the paper [47]. The reconstruction results is shown in Figure 5(c). It is demonstrated that final resolution is 3.20Å, which is derived by FSC curve in figure 5(d) using the same 0.143 cutoff (dashed line) to choose the final resolution. We note that the final resolution by RELION after denoising is as good as the original resolution 3.20Å reported in [47].

4 Conclusion and Discussion

In this paper, we set a connection between the traditional image forward model and Huber contamination model in solving the complex contamination in the Cryo-EM dataset. we have seen that joint training of Autoencoder and GAN can substantially improve the performance in Cryo-EM image denoising. In this joint training scheme, on the one hand, the reconstruction loss of Autoencoder helps GAN to avoid mode collapse and stabilize training; on the other hand, GAN helps Autoencoder in denoising by utilizing the highly correlated Cryo-EM images since they are 2D projections of one or a few 3D molecular conformations. To overcome the low signal-noise-ratio challenge in Cryo-EM images, joint training of ℓ_1 Autoencoder combined with (.5, .5)-GAN, (1, 1)-GAN, and WGAN with gradient penalty is often among the best performance in terms of MSE, PSNR, and SSIM when the data is contamination-free. However, when a portion of data is contaminated, especially when the reference data is contaminated, WGAN with ℓ_1 Autoencoder may suffer from the significant deterioration of reconstruction accuracy. Therefore, robust ℓ_1 Autoencoder combined with robust GANs ((.5, .5)-GAN and (1, 1)-GAN) are the overall best choices for robust denoising with contaminated and high noise datasets.

There are also some related work. Most of the deep learning-based techniques in image denoising need reference data, limiting themselves in the application of Cryo-EM denoising. For example, in our experimental dataset EMPIRE-10028, the reference data is generated by the cryoSPARC, which itself becomes problematic in highly heterogeneous conformations. Therefore the reference image we learn may follow a fake distribution. How to denoise without the reference image thus becomes a significant problem. It is still open how to adapt to different experiments and those without reference images. In order to overcome this drawback, an idea called “image-blind denoising” is offered by [27, 25], they view the noisy image or void image as the reference image to denoise. Besides, [11] tries to extract the noise distribution from the noisy image and gain denoised images through removing the noise for noisy data; [35] augments the data by Bernoulli sampling and denoise image with dropout. Besides, [7] applies noise2noise into Cryo-EM image denoising. Nevertheless, all of the methods need noise is independent of the elements themselves. Thus it is hard to remove noise in Cryo-EM because the noise from ice and machine is related to the particles.

What is more, for reconstruction problems in Cryo-EM, [52] proposes an end-to-end 3D reconstruction approach based on the network from Cryo-EM images, where they attempt to borrow the variational Autoencoder (VAE) to approximate the forward reconstruction model and recover the 3D structure directly by combining the angle information and image information learned from data. This is one future direction to pursue.

Acknowledgment

X.H. acknowledges support from the Hong Kong Research Grant Council (T13-605/18-W, AoE/M-09/12 and AoE/P-705/16) and Innovation and Technology Commission (ITCPD/17-9). The research of Y. Y. was supported in part by Hong Kong Research Grant Council (HKRGC) grant 16303817, ITF UIM/390, as well as awards from Tencent AI Lab, Si Family Foundation, and Microsoft Research-Asia.

5 Appendix

5.1 Robust Estimate via β -GAN

In this paper, we extend the traditional image generative model in Cryo-EM to a Huber contamination model and exploit the β -GAN toward robust denoising under unknown contamination. Below we include a brief introduction to robust β -GAN, which achieves provable robust estimate or recovery under Huber contamination model. Recently, [16] and [17] established the statistical optimality of β -GANs for robust estimate of mean (location) and covariance (scatter) of the general elliptical distributions. Here we introduce the main results that will be helpful in this paper.

Definition 1 (Elliptical Distribution). *A random vector $X \in \mathbb{R}^p$ follows an elliptical distribution if and only if it has the representation $X = \theta + \xi AU$, where $\theta \in \mathbb{R}^p$ and $A \in \mathbb{R}^{p \times r}$ are model parameters. The random variable U is distributed uniformly on the unit sphere $\{u \in \mathbb{R}^r : \|u\| = 1\}$ and $\xi \geq 0$ is a random variable in \mathbb{R} independent of U . The vector θ and the matrix $\Sigma = AA^T$ are called the location and the scatter of the elliptical distribution.*

Normal distribution is just a member in this family characterized by mean θ and covariance matrix Σ . Cauchy distribution is another member in this family whose moments do not exist.

Definition 2 (Huber contamination model). $X_1, \dots, X_n \sim^{iid} (1 - \epsilon)P_{ell} + \epsilon Q$, where in this paper we consider the P_{ell} an elliptical distribution in its canonical form.

A more general data generating process than Huber contamination model is called the strong contamination model below, as the TV-neighborhood of a given elliptical distribution P_{ell} :

Definition 3 (Strong contamination model). $X_1, \dots, X_n \sim^{iid} P$, for some P satisfying

$$TV(P, P_{ell}) < \epsilon.$$

Definition 4 (Discriminator Class). Let $\text{sigmoid}(x) = \frac{1}{1+e^{-x}}$, $\text{ramp}(x) = \max(\min(x + 1/2, 1), 0)$, and $\text{ReLU}(x) = \max(x, 0)$. Define a general discriminator class of deep neural nets: firstly define the a ramp bottom layer

$$\mathcal{G}_{\text{ramp}} = g(x) = \text{ramp}(u^t x + b), u \in \mathbb{R}^p, b \in \mathbb{R} \quad (9)$$

Then, with $\mathcal{G}_1(B) = \mathcal{G}_{\text{ramp}}$, inductively define

$$\mathcal{G}_{l+1}(B) = \left\{ g(x) = \text{ReLU} \left(\sum_{h \geq 1} v_h g_h(x) \right) : \sum_{h \geq 1} |v_h| \leq B, g_h \in \mathcal{G}_l(B) \right\} \quad (10)$$

Noted that the neighboring two layers are connected via ReLU activation functions. Finally, the network structure is defined by:

$$\mathcal{D}^L(\kappa, B) = \left\{ D(x) = \text{sigmoid} \left(\sum_{j \geq 1} w_j g_j(x) \right) : \sum_{j \geq 1} |w_j| \leq \kappa, g_j \in \mathcal{G}_L(B) \right\} \quad (11)$$

This is a neural network classes consists of L hidden layers.

Now consider the following β -GAN induced by a proper scoring rule $S : [0, 1] \times \{0, 1\} \rightarrow \mathbb{R}$ with the discriminator class above:

$$(\hat{\theta}, \hat{\Sigma}) = \arg \min_{(\theta, \Sigma)} \max_{D \in \mathcal{D}^L(\kappa, B)} \frac{1}{n} \sum_{i=1}^n S(D(x_i), 1) + \mathbb{E}_{x \sim P_{ell}(\Theta, \Sigma)} S(D(x), 0). \quad (12)$$

The following theorem shows that such a β -GAN may give a statistically optimal estimate of location and scatter of the general family of Elliptical distributions under strong contamination models.

Theorem 1 (Gao-Yao-Zhu, citepgao2019generative). *Consider the (α, β) -GANs with $|\alpha - \beta| < 1$. The discriminator class $D = \mathcal{D}^L(k, B)$ is specified by (11). Assume $\frac{p}{n} + \epsilon^2 \leq c$ for some sufficiently small constant $c > 0$. Set $1 \leq L = O(1)$, $1 \leq B = O(1)$, and $\kappa = O(\sqrt{\frac{p}{n}} + \epsilon)$. Then for any $X_1, \dots, X_n \sim^{iid} P$, for some P satisfying $TV(P, P_{ell}) < \epsilon$ with small enough ϵ , we have:*

$$\begin{aligned} \|\hat{\theta} - \theta\|^2 &< C \left(\frac{p}{n} \vee \epsilon^2 \right) \\ \|\hat{\Sigma} - \Sigma\|_{op}^2 &< C \left(\frac{p}{n} \vee \epsilon^2 \right) \end{aligned} \quad (13)$$

with probability at least $1 - e^{C'(p+n\epsilon^2)}$ (universal constants C and C') uniformly over all $\theta \in \mathbb{R}^p$ and all $\|\Sigma\|_{op} \leq M$.

The theorem established that for all $|\alpha - \beta| < 1$, (α, β) -GAN family is robust in the sense that one can learn a distribution P_{ell} from contaminated distributions P_ϵ such that $TV(P_\epsilon, P_{ell}) < \epsilon$, which includes Huber contamination model as a special case. Therefore a (α, β) -GAN with suitable choice of network architecture, can robustly learn the generative model from arbitrary contamination Q when ϵ is small (e.g. no more than 1/3).

This theoretical development is the inspiration of current work on Cryo-EM robust denoising problem. In our case, we hope that the denoising Autoencoder network $G_\theta(y)$ can provide us a universal approximation of the location (mean) of the inverse generative model (1), where the noise can be any member of the elliptical distribution. Moreover, our discriminator is adapted to the image classification problem in our case. Equipped with this design, we hope that the (α, β) -GANs adopted in this paper may help enhance the robustness of denoising Autoencoder against unknown contaminations, e.g. the Huber contamination model for real contamination in Cryo-EM data. The experimental results in this paper in fact confirms the efficacy of such a design.

5.2 Stability of combining Autoencoder into GAN

We emphasize that in this joint training of Autoencoder and GAN scheme, not only GANs could help Autoencoder by exploiting information from similar samples, but also Autoencoder is indispensable to GANs in stabilizing the training of the latter. As a zero-sum game involving a non-convex-concave minimax optimization problem, training GANs is notoriously unstable with typical cyclic dynamics and possible mode collapse entrapped by local optima. However, the introduction of Autoencoder loss here is able to stabilize the training and avoid the mode collapse.

As an illustration, Figure 6 shows the comparison of training a JSGAN and a joint JSGAN- ℓ_1 Autoencoder. Training and test mean square error curves are plotted against iteration numbers, using the RNAP data under $SNR = 0.1$ that will be introduced later. From this figure, one can see that JSGAN training suffers from drastic oscillations while joint training of JSGAN- ℓ_1 Autoencoder exhibits a stable process. In fact, with the aid of Autoencoder here, one does not need the popular “log D trick” in JSGAN.

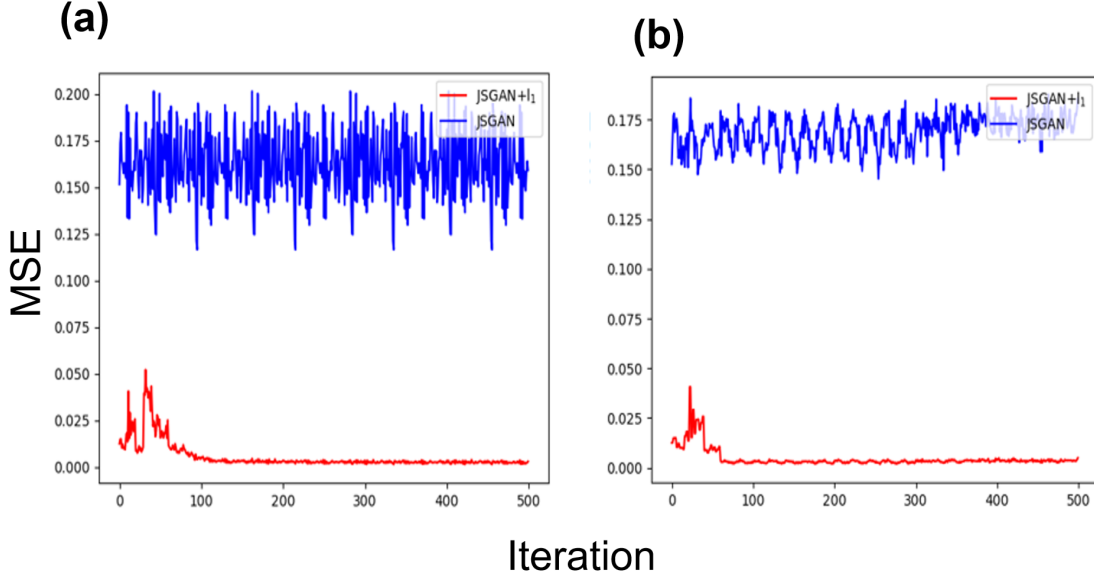


Figure 6: Comparison between JSGAN (blue) and joint JSGAN- ℓ_1 Autoencoder (red). (a) training MSE; (b) test MSE. Joint training of JSGAN- ℓ_1 Autoencoder is much more stable than pure JSGAN training that oscillates a lot.

5.3 Influence of parameter (α, β) brings in β -GAN

In the paper, we have applied β -GAN into denoising problem. How to pick up a good parameter: (α, β) in the β -GAN becomes an important issue. In this part, we research the impact of the parameter (α, β) on the outcome. We choose eight significant groups of α, β . Our result is shown in Table 2. It is demonstrated that the effect of these groups in different parameters is not large. The best result appears in $\alpha = 1, \beta = 1$ and $\alpha = 0.5, \beta = 0.5$

Table 2: ResNet-GAN: MSE, PSNR and SSIM of different (α, β) in β -GAN under various levels of Gaussian noise corruption in RNAP dataset.

Parameter/SNR	MSE		PSNR		SSIM	
	0.1	0.05	0.1	0.05	0.1	0.05
$\alpha = 1, \beta = 1$	2.99e-3(3.51e-5)	4.01e-3(1.54e-4)	25.30(0.05)	24.07(0.16)	0.82(0.03)	0.79(0.03)
$\alpha = 0.5, \beta = 0.5$	3.01e-3(2.81e-5)	3.98e-3(4.60e-5)	25.27(0.04)	24.07(0.05)	0.79(0.04)	0.80(0.03)
$\alpha = -0.5, \beta = -0.5$	3.02e-3(1.69e-5)	4.15e-3(5.05e-5)	25.27(0.02)	23.91(0.05)	0.80(0.03)	0.80(0.03)
$\alpha = -1, \beta = -1$	3.05e-3(3.54e-5)	4.12e-3(8.30e-5)	25.23(0.05)	23.93(0.08)	0.80(0.05)	0.77(0.04)
$\alpha = 1, \beta = -1$	3.05e-3(4.30e-5)	4.10e-3(5.80e-5)	25.24(0.06)	23.96(0.06)	0.82(0.02)	0.76(0.03)
$\alpha = 0.5, \beta = -0.5$	3.09e-3(6.79e-5)	4.05e-3(6.10e-5)	25.17(0.04)	24.01(0.06)	0.79(0.04)	0.77(0.05)
$\alpha = 0, \beta = 0$	3.06e-3(5.76e-5)	4.02e-3(5.67e-4)	25.23(0.04)	24.00(0.06)	0.78(0.03)	0.78(0.03)
$\alpha = 0.1, \beta = -0.1$	3.07e-3(5.62e-5)	4.05e-3(8.55e-5)	25.23(0.08)	23.98(0.04)	0.78(0.02)	0.79(0.03)

5.4 Clustering to solve the conformational heterogeneity

In this section, we try to analyze whether the denoised result is good in solving conformation heterogeneity in simulated RNAP dataset. Specifically, for heterogeneous conformations in simulation data, we mainly choose the following two typical conformations: *open* and *close* conformations as our testing data. Our goal is to distinguish these two classes of conformations. However, different from [48], we do not have the template images to calculate the distance matrix, so what we try is unsupervised learning – clustering. Our clustering method is firstly using manifold learning: Isomap [40] to reduce the dimension of the denoised images, then make use of k -Means ($k = 2$) to group the different conformations.

The Figure 7(a) displays the 2D visualizations of two conformations about the clustering effect in different denoised methods. Here we set the SNR of noisy data is 0.05. In correspondence to those visualizations, the accuracy of competitive methods is reported here: (1, 1)-GAN+ ℓ_1 : 54/60 (54 clustering correctly in 60), WGANgp+ ℓ_1 : 54/60, ℓ_2 -Autoencoder: 44/60, BM3D: 34/60, and KSVD: 36/60. This experiment shows that: clean images separate well; (α, β) -GAN and WGANgp with ℓ_1 Autoencoder can distinguish the open and close structure partially, although there exists several wrong points; ℓ_2 -Autoencoder and traditional techniques have poor performance because it is hard to detect the clamp shape.

Furthermore, the reason we use Isomap is it performs the best in our case and comparisons of different manifold learning methods are shown in Figure 7(b). It demonstrates that blue and red points separate most in the graph of ISOMAP. Specifically, the accuracy of these four methods are 50/60 (spectral method), 46/50 (MDS), 46/50 (TSNE), and 54/60 (ISOMAP). it shown that Isomap can distinguish best in the two structures’ images compared to other methods: such as the Spectral method [32], MDS [12], and TSNE [28].

5.5 Convolution network

In this part, we will present the result of simple deep convolution network (remove the ResNet block), the performances in all of criterion are worse than performances of the residue’s architecture work. Table 3 compares the MSE and PSNR performance of various methods in the RNAP dataset with SNR 0.1 and 0.05. And Figure 8(a) displays the denoised image of different methods in the RNAP dataset with SNR 0.05. It shows the advantage of residue structure in our GAN-based denoising Cryo-EM problem.

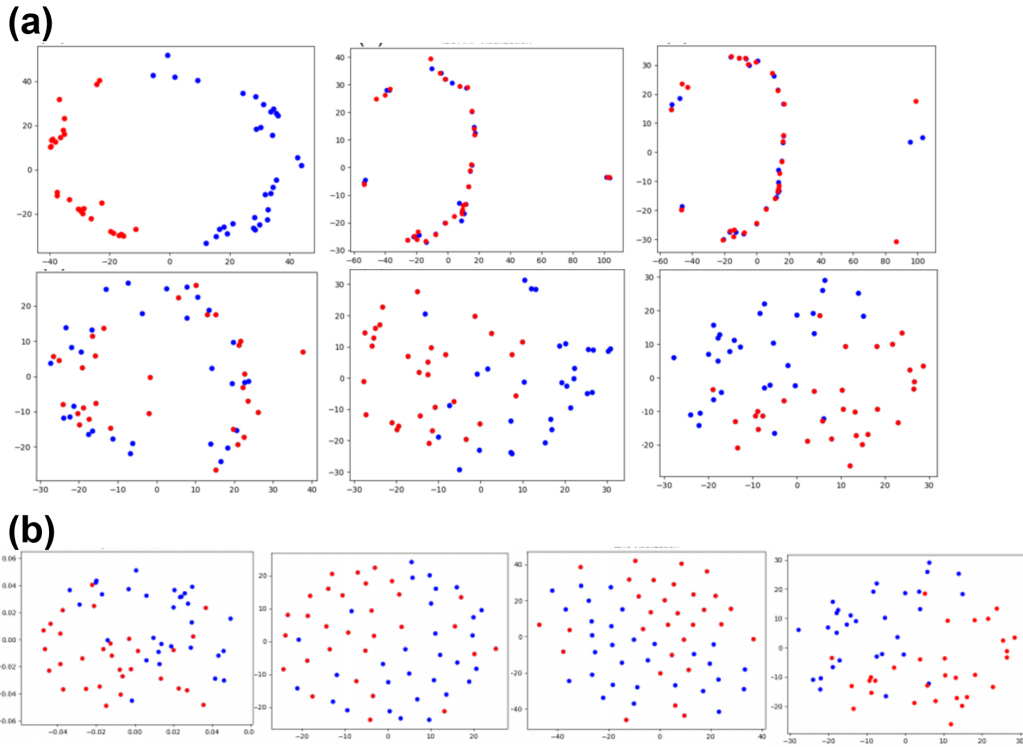


Figure 7: 2D visualization of 2-conformational images. Red point, blue point separately represent the open and closed conformation. (a) is 2D visualization of 2-conformation image by ISOMAP in different methods (from the left and top to the right and bottom): clean image, BM3D, KSVD, ℓ_2 -Autoencoder, (1,1)-GAN+ ℓ_1 , WGANgp+ ℓ_1 . (b) is 2D visualization of 2-conformation image in different manifold learning methods (from left to right): Spectral methods, MDS, TSNE, and ISOMAP.

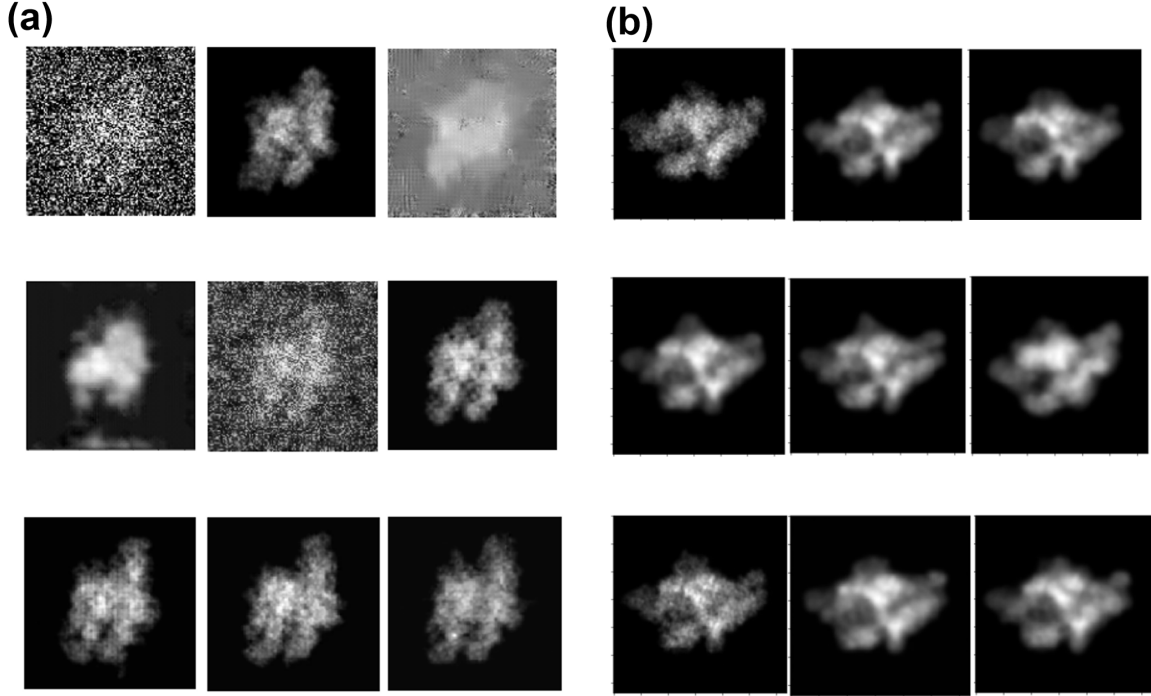


Figure 8: (a) Denoised images with convolution network without resnet structure in different methods in RNAP dataset with SNR 0.05 (from left to right, top to bottom): clean, noisy, BM3D, ℓ_2 -Autoencoder, KSVD, JSGAN + ℓ_1 , WGANgp + ℓ_1 , (1, -1)-GAN + ℓ_1 , (.5, -.5)-GAN + ℓ_1 . (b) Denoised and reference images in different regularization λ (we use (.5, -.5)-GAN + $\lambda \ell_1$ as an example) in corresponding to Table 4. From left to right, top to bottom, the image is: Clean image, $\lambda = 0.1$, $\lambda = 1$, $\lambda = 5$, $\lambda = 10$, $\lambda = 50$, $\lambda = 100$, $\lambda = 500$, $\lambda = 10000$

Table 3: Deep convolution results: MSE and PSNR of different models under various levels of Gaussian noise corruption in RNAP dataset.

Method/SNR	MSE		PSNR	
	0.1	0.05	0.1	0.05
BM3D	3.5e-2 (7.8e-3)	5.9e-2(9.9e-3)	14.535(0.1452)	12.134(0.1369)
KSVD	1.8e-2(6.6e-3)	3.5e-2(7.6e-3)	17.570(0.1578)	14.609(0.1414)
Non-local means	5.0e-2(5.5e-3)	5.8e-2(8.9e-3)	13.040(0.4935)	12.404(0.6498)
CWF	2.5e-2(2.0e-3)	9.3e-3(8.8e-4)	16.059(0.3253)	20.314(0.4129)
ℓ_2 -Autoencoder	4.0e-3(6.0e-4)	6.7e-3(9.0e-4)	24.202(0.6414)	21.739(0.7219)
(0,0)-GAN + ℓ_1	3.8e-3(6.0e-4)	5.6e-3(8.0e-4)	24.265(0.6537)	22.594(0.6314)
WGANgp+ ℓ_1	3.1e-3(5.0e-4)	5.0e-3(8.0e-4)	25.086(0.6458)	23.010(0.6977)
(1, -1)-GAN + ℓ_1	3.4e-3(5.0e-4)	4.9e-3(9.0e-4)	24.748(0.7233)	23.116(0.7399)
(.5, -.5)-GAN + ℓ_1	3.5e-3(5.0e-4)	5.6e-3(9.0e-4)	24.556(0.6272)	22.575(0.6441)

5.6 PGGAN experiment

In this section, we use one of the popular GAN training skills: PGGAN to denoise. Our experiments partially demonstrate two things: 1) the denoised images sharpen more, though the MSE changes to be higher. 2) we do not need to add ℓ_1 regularization to make model training stable; it also can detect the outlier of images for both real data and simulated data without regularization.

We apply WGANgp into the RNAP simulated dataset with SNR 0.05 as an example to explain. The denoised images are presented in Figure 9 ; it is noted that the model is hard to collapse regardless of adding ℓ_1 regularization. The MSE of adding regularization is $8.09e-3(1.46e-3)$ is less than $1.01e-2(1.81e-3)$ without adding regularization. Nevertheless, both of them don't exceed the GAN result based on the ResNet structure. The reason lies in that architecture doesn't borrow the strengths of the ResNet structure. But an advantage of PGGAN lies in its efficiency in training. So it is an interesting open problem to improve PGGAN toward the accuracy of ResNet based GANs.

Another thing that needs to highlight is that MSE may not be a good criterion because denoised images by PGGAN are clearer in some details than the front methods we propose. This phenomenon is also shown in Appendix 5.7. So how to find a better criterion to evaluate the model and combine two strengths of ResNet-GAN and PGGAN await us to explore.

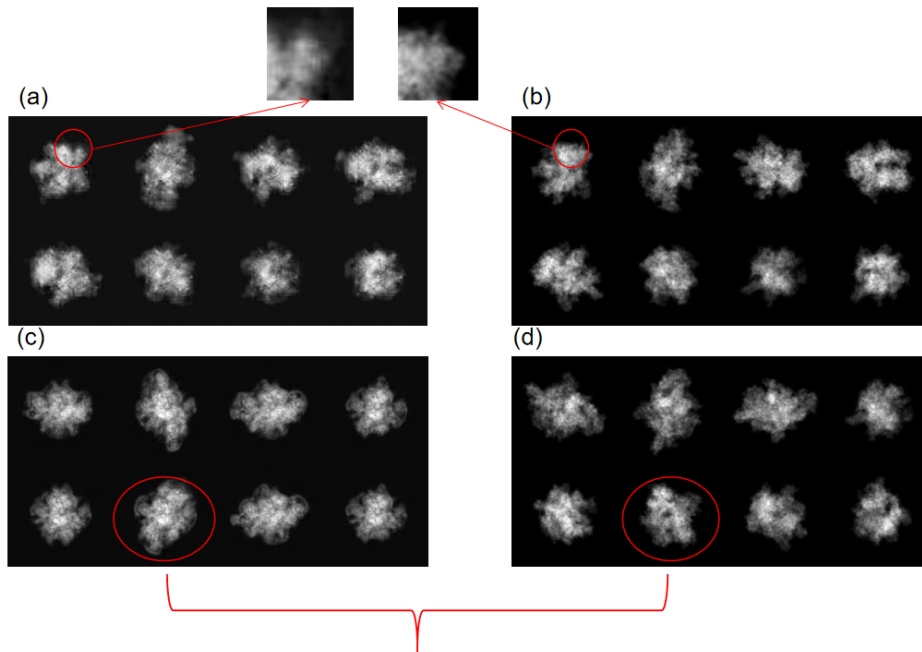


Figure 9: Denoised and reference images by PGGAN in RNAP dataset. (a) WGANgp + ℓ_1 denoise (b) WGANgp + ℓ_1 reference (c) WGANgp denoise (d) WGANgp reference.

5.7 Influence of the regularization parameter: λ

In this paper, we add ℓ_1 regularization to make model stable, but how to choose λ of ℓ_1 regularization becomes a significant problem. Here we take (.5, .5)-GAN to denoise in RNAP dataset with SNR 0.1. According to some results in different λ in Table 4, we find as the λ tends to infinity, the MSE results tends to ℓ_1 -Autoencoder, which is reasonable. Also, the MSE result becomes the smallest as the $\lambda = 10$.

What’s more, we find a interesting phenomenon that picture becomes much clearer at $\lambda = 100$ than that at $\lambda = 10$, although the MSE is not the best (shown in the Figure 8(b)).

Table 4: MSE, PSNR and SSIM of different λ in (.5,.5)-GAN + $\lambda\ell_1$ in RNAP dataset.

λ /criterion	MSE	PSNR	SSIM
0.1	3.06e-3(4.50e-5)	25.22(0.07)	0.82(0.06)
1	3.05e-3(4.49e-5)	25.24(0.06)	0.81(0.05)
5	3.03e-3(2.80e-5)	25.26(0.04)	0.80(0.04)
10	3.01e-3(2.81e-5)	25.27(0.04)	0.79(0.04)
50	3.07e-3(3.95e-5)	25.20(0.06)	0.79(0.02)
100	3.11e-3(5.96e-5)	25.15(0.06)	0.80(0.02)
500	3.17e-3(5.83e-5)	25.01(0.07)	0.78(0.04)
10000	3.17e-3(2.90e-5)	25.03(0.04)	0.79(0.04)

References

- [1] Forest Agostinelli, Michael R Anderson, and Honglak Lee. Adaptive multi-column deep neural networks with application to robust image denoising. In *Advances in Neural Information Processing Systems*, pages 1493–1501, 2013.
- [2] Michal Aharon, Michael Elad, and Alfred Bruckstein. K-svd: An algorithm for designing overcomplete dictionaries for sparse representation. *IEEE Transactions on signal processing*, 54(11):4311–4322, 2006.
- [3] Martin Arjovsky, Soumith Chintala, and Léon Bottou. Wasserstein gan. *arXiv preprint arXiv:1701.07875*, 2017.
- [4] Brian Bae, Andrey Feklistov, Agnieszka Lass-Napiorkowska, Robert Landick, and Seth A Darst. Structure of a bacterial rna polymerase holoenzyme open promoter complex. *Elife*, 4:e08504, 2015.
- [5] Chen Bai, Meiling Zhou, Junwei Min, Shipei Dang, Xianghua Yu, Peng Zhang, Tong Peng, and Baoli Yao. Robust contrast-transfer-function phase retrieval via flexible deep learning networks. *Optics letters*, 44(21):5141–5144, 2019.
- [6] Xiao-Chen Bai, Greg McMullan, and Sjors HW Scheres. How cryo-em is revolutionizing structural biology. *Trends in biochemical sciences*, 40(1):49–57, 2015.
- [7] Tristan Bepler, Kotaro Kelley, Alex J Noble, and Bonnie Berger. Topaz-denoise: general deep denoising models for cryoem and cryoet. *Nature communications*, 11(1):1–12, 2020.

- [8] Tejal Bhamre, Teng Zhang, and Amit Singer. Denoising and covariance estimation of single particle cryo-em images. *Journal of structural biology*, 195(1):72–81, 2016.
- [9] Douglas F Browning and Stephen JW Busby. The regulation of bacterial transcription initiation. *Nature Reviews Microbiology*, 2(1):57–65, 2004.
- [10] James Chen, Courtney Chiu, Saumya Gopalkrishnan, Albert Y Chen, Paul Dominic B Olinares, Ruth M Saecker, Jared T Winkelman, Michael F Maloney, Brian T Chait, Wilma Ross, et al. Stepwise promoter melting by bacterial rna polymerase. *Molecular Cell*, 2020.
- [11] Jingwen Chen, Jiawei Chen, Hongyang Chao, and Ming Yang. Image blind denoising with generative adversarial network based noise modeling. In *Proceedings of the IEEE Conference on Computer Vision and Pattern Recognition*, pages 3155–3164, 2018.
- [12] Michael AA Cox and Trevor F Cox. Multidimensional scaling. In *Handbook of data visualization*, pages 315–347. Springer, 2008.
- [13] Kostadin Dabov, Alessandro Foi, Vladimir Katkovnik, and Karen Egiazarian. Image denoising by sparse 3-d transform-domain collaborative filtering. *IEEE Transactions on image processing*, 16(8):2080–2095, 2007.
- [14] Joachim Frank. Two-dimensional averaging techniques. *Three-Dimensional Electron Microscopy of Macromolecular Assemblies: Visualization of Biological Molecules in Their Native State*, pages 131–144, 1996.
- [15] Joachim Frank. *Three-dimensional electron microscopy of macromolecular assemblies: visualization of biological molecules in their native state*. Oxford University Press, 2006.
- [16] Chao Gao, Jiyi Liu, Yuan Yao, and Weizhi Zhu. Robust estimation and generative adversarial nets. In *International Conference on Learning Representations (ICLR), New Orleans, Louisiana, United States*. 2019. arXiv preprint arXiv:1810.02030.
- [17] Chao Gao, Yuan Yao, and Weizhi Zhu. Generative adversarial nets for robust scatter estimation: A proper scoring rule perspective. *Journal of Machine Learning Research*, *accepted*, 2019. arXiv preprint arXiv:1903.01944.
- [18] Ian Goodfellow, Jean Pouget-Abadie, Mehdi Mirza, Bing Xu, David Warde-Farley, Sherjil Ozair, Aaron Courville, and Yoshua Bengio. Generative adversarial nets. In *Advances in neural information processing systems*, pages 2672–2680, 2014.
- [19] Ishaan Gulrajani, Faruk Ahmed, Martin Arjovsky, Vincent Dumoulin, and Aaron C Courville. Improved training of wasserstein gans. In *Advances in neural information processing systems*, pages 5767–5777, 2017.
- [20] Peter J Huber. Robust estimation of a location parameter. In *Breakthroughs in statistics*, pages 492–518. Springer, 1992.
- [21] Tero Karras, Timo Aila, Samuli Laine, and Jaakko Lehtinen. Progressive growing of gans for improved quality, stability, and variation. *arXiv preprint arXiv:1710.10196*, 2017.

- [22] Hiroo Kenzaki, Nobuyasu Koga, Naoto Hori, Ryo Kanada, Wenfei Li, Kei-ichi Okazaki, Xin-Qiu Yao, and Shoji Takada. Cafemol: A coarse-grained biomolecular simulator for simulating proteins at work. *Journal of Chemical Theory and Computation*, 7(6):1979–1989, 2011.
- [23] Diederik P Kingma and Jimmy Ba. Adam: A method for stochastic optimization. *arXiv preprint arXiv:1412.6980*, 2014.
- [24] Georgii G Krivov, Maxim V Shapovalov, and Roland L Dunbrack Jr. Improved prediction of protein side-chain conformations with scwrl4. *Proteins: Structure, Function, and Bioinformatics*, 77(4):778–795, 2009.
- [25] Alexander Krull, Tim-Oliver Buchholz, and Florian Jug. Noise2void-learning denoising from single noisy images. In *Proceedings of the IEEE Conference on Computer Vision and Pattern Recognition*, pages 2129–2137, 2019.
- [26] Werner Kühlbrandt. The resolution revolution. *Science*, 343(6178):1443–1444, 2014.
- [27] Jaakko Lehtinen, Jacob Munkberg, Jon Hasselgren, Samuli Laine, Tero Karras, Miika Aittala, and Timo Aila. Noise2noise: Learning image restoration without clean data. *arXiv preprint arXiv:1803.04189*, 2018.
- [28] Laurens van der Maaten and Geoffrey Hinton. Visualizing data using t-sne. *Journal of machine learning research*, 9(Nov):2579–2605, 2008.
- [29] R Marabini, IM Masegosa, MC San Martín, S Marco, JJ Fernandez, LG De la Fraga, C Vaquerizo, and JM Carazo. Xmipp: an image processing package for electron microscopy. *Journal of structural biology*, 116(1):237–240, 1996.
- [30] Benjamin L Moore, Lawrence A Kelley, James Barber, James W Murray, and James T MacDonald. High-quality protein backbone reconstruction from alpha carbons using gaussian mixture models. *Journal of computational chemistry*, 34(22):1881–1889, 2013.
- [31] Katsuhiko S Murakami, Shoko Masuda, and Seth A Darst. Structural basis of transcription initiation: Rna polymerase holoenzyme at 4 Å resolution. *Science*, 296(5571):1280–1284, 2002.
- [32] Andrew Y Ng, Michael I Jordan, and Yair Weiss. On spectral clustering: Analysis and an algorithm. In *Advances in neural information processing systems*, pages 849–856, 2002.
- [33] Kei-ichi Okazaki, Nobuyasu Koga, Shoji Takada, Jose N Onuchic, and Peter G Wolynes. Multiple-basin energy landscapes for large-amplitude conformational motions of proteins: Structure-based molecular dynamics simulations. *Proceedings of the National Academy of Sciences*, 103(32):11844–11849, 2006.
- [34] Ali Punjani, John L Rubinstein, David J Fleet, and Marcus A Brubaker. cryosparc: algorithms for rapid unsupervised cryo-em structure determination. *Nature methods*, 14(3):290, 2017.

- [35] Yuhui Quan, Mingqin Chen, Tongyao Pang, and Hui Ji. Self2self with dropout: Learning self-supervised denoising from single image. In *Proceedings of the IEEE/CVF Conference on Computer Vision and Pattern Recognition*, pages 1890–1898, 2020.
- [36] Sjors HW Scheres. Relion: implementation of a bayesian approach to cryo-em structure determination. *Journal of structural biology*, 180(3):519–530, 2012.
- [37] Sjors HW Scheres. Processing of structurally heterogeneous cryo-em data in relion. In *Methods in enzymology*, volume 579, pages 125–157. Elsevier, 2016.
- [38] Peter S Shen. The 2017 nobel prize in chemistry: cryo-em comes of age. *Analytical and bioanalytical chemistry*, 410(8):2053–2057, 2018.
- [39] Min Su, Hantian Zhang, Kevin Schawinski, Ce Zhang, and Michael A Cianfrocco. Generative adversarial networks as a tool to recover structural information from cryo-electron microscopy data. *BioRxiv*, page 256792, 2018.
- [40] Joshua B Tenenbaum, Vin De Silva, and John C Langford. A global geometric framework for nonlinear dimensionality reduction. *science*, 290(5500):2319–2323, 2000.
- [41] John W Tukey. Mathematics and the picturing of data. In *Proceedings of the International Congress of Mathematicians, Vancouver, 1975*, volume 2, pages 523–531, 1975.
- [42] Pascal Vincent, Hugo Larochelle, Yoshua Bengio, and Pierre-Antoine Manzagol. Extracting and composing robust features with denoising autoencoders. In *Proceedings of the 25th international conference on Machine learning*, pages 1096–1103. ACM, 2008.
- [43] Feng Wang, Huichao Gong, Gaochao Liu, Meijing Li, Chuangye Yan, Tian Xia, Xueming Li, and Jianyang Zeng. Deeppicker: A deep learning approach for fully automated particle picking in cryo-em. *Journal of structural biology*, 195(3):325–336, 2016.
- [44] Jia Wang and ChangCheng Yin. A zernike-moment-based non-local denoising filter for cryo-em images. *Science China Life Sciences*, 56(4):384–390, 2013.
- [45] Zhou Wang, Alan C Bovik, Hamid R Sheikh, and Eero P Simoncelli. Image quality assessment: from error visibility to structural similarity. *IEEE transactions on image processing*, 13(4):600–612, 2004.
- [46] Dai-Yu Wei and Chang-Cheng Yin. An optimized locally adaptive non-local means denoising filter for cryo-electron microscopy data. *Journal of structural biology*, 172(3):211–218, 2010.
- [47] Wilson Wong, Xiao-chen Bai, Alan Brown, Israel S Fernandez, Eric Hanssen, Melanie Condron, Yan Hong Tan, Jake Baum, and Sjors HW Scheres. Cryo-em structure of the plasmodium falciparum 80s ribosome bound to the anti-protozoan drug emetine. *Elife*, 3:e03080, 2014.
- [48] Yin Xian, Hanlin Gu, Wei Wang, Xuhui Huang, Yuan Yao, Yang Wang, and Jian-Feng Cai. Data-driven tight frame for cryo-em image denoising and conformational classification. In *2018 IEEE Global Conference on Signal and Information Processing (GlobalSIP)*, pages 544–548. IEEE, 2018.

- [49] Junyuan Xie, Linli Xu, and Enhong Chen. Image denoising and inpainting with deep neural networks. In *Advances in neural information processing systems*, pages 341–349, 2012.
- [50] Qingsong Yang, Pingkun Yan, Yanbo Zhang, Hengyong Yu, Yongyi Shi, Xuanqin Mou, Mannudeep K Kalra, Yi Zhang, Ling Sun, and Ge Wang. Low-dose ct image denoising using a generative adversarial network with wasserstein distance and perceptual loss. *IEEE transactions on medical imaging*, 37(6):1348–1357, 2018.
- [51] Kai Zhang, Wangmeng Zuo, Yunjin Chen, Deyu Meng, and Lei Zhang. Beyond a gaussian denoiser: Residual learning of deep cnn for image denoising. *IEEE Transactions on Image Processing*, 26(7):3142–3155, 2017.
- [52] Ellen D Zhong, Tristan Bepler, Joseph H Davis, and Bonnie Berger. Reconstructing continuous distributions of 3d protein structure from cryo-em images. In *ICLR*, 2020.